

Numerical Study on the Along-Track Interferometric Radar Imaging Mechanism of Oceanic Surface Currents

Roland Romeiser and Donald R. Thompson

Abstract—The phase information in along-track interferometric synthetic aperture radar (along-track INSAR, ATI) images is a measure of the Doppler shift of the backscattered signal and thus of the line-of-sight velocity of the scatterers. It can be exploited for oceanic surface current measurements from aircraft or spacecraft. However, as already discussed in previous publications, the mean Doppler frequency of the radar backscatter from the ocean is not exclusively determined by the mean surface current, but it includes contributions associated with surface wave motion. In this paper, we present an efficient new model for the simulation of Doppler spectra and ATI signatures. The model is based on Bragg scattering theory in a composite surface model approach. We show that resulting Doppler spectra are consistent with predictions of an established model based on fundamental electrodynamic expressions, while computation times are reduced by more than one order of magnitude. This can be a key advantage with regard to operational applications of ATI. Based on model calculations for two simple current fields and various wind conditions and radar configurations, we study theoretical possibilities and limitations of oceanic current measurements by ATI. We find that best results can be expected from ATI systems operated at high microwave frequencies like 10 GHz (X band), high incidence angles like 60° , low platform altitude/speed ratios, and vertical (VV) polarization. The ATI time lag should be chosen long enough to obtain measurable phase differences, but much shorter than the decorrelation time of the backscattered field.

Index Terms—Doppler spectra, interferometry, ocean currents, remote sensing, synthetic aperture radar (SAR).

I. INTRODUCTION

THE FREQUENCY of a radar signal which is backscattered by a moving target experiences a Doppler shift proportional to the target's line-of-sight velocity. The Doppler spectrum of the radar return from the ocean surface, as detected by coherent microwave radars, reflects the distribution of the line-of-sight velocity of the scatterers, weighted by their contributions to the backscattered power. The first moment of the Doppler spectrum, the mean Doppler frequency or Doppler offset, corresponds to a power-weighted mean line-of-sight ve-

locity of the scatterers. The variance of the velocity distribution determines the bandwidth of the Doppler spectrum.

Aside from statistical fluctuations, along-track interferometric synthetic aperture radar (along-track INSAR, ATI) systems can directly detect the Doppler offset associated with each pixel of a synthetic aperture radar (SAR) image. This is achieved by interferometric combination of two complex SAR images of the same scene which are acquired with a short time lag τ by two antennas separated along the flight track [1]. If τ is short compared to the decorrelation time of the backscattered field, the expectation value of the phase difference between corresponding pixels in the two images is determined by the Doppler offset of the signal mapped into those pixels. The ATI technique is promising for quasisynoptic measurements of spatial surface current variations on scales of meters within areas of many square kilometers, including the orbital currents of long ocean waves that are resolved by the radar. In conventional radar intensity images, such features become visible only via hydrodynamic modulation of the surface roughness and tilt modulation of the local incidence angle.

However, the Doppler offset, and thus the ATI image phase, is not simply proportional to the component of the mean surface current parallel to the radar look direction. It includes contributions associated with the phase velocity of the short "Bragg" waves that give rise to resonant Bragg scattering [2], [3] and, via higher-order effects, with the orbital motions of all ocean waves which are long compared to the Bragg scattering facets and which modulate the backscattered signal in amplitude and frequency. Although comparisons of simultaneously acquired radar and *in situ* data have shown relatively good agreement in cases where no strong current gradients were present [4], other studies where ATI-derived current variations over oceanic internal waves were compared with *in situ* measurements have found significant discrepancies [5]. Also a clear dependence of observed Doppler offsets on the polarization of the radar, which is well known from Doppler scatterometer measurements, indicates that nonzero-mean subresolution scale effects exist which must not be neglected when converting Doppler offsets or ATI image phases into surface currents.

Measured Doppler spectra can be explained relatively well by fundamental radar backscattering models based explicitly on Maxwell's equations [6]. Such models are quite complex, and computations are time-consuming, since the time-dependent autocorrelation function of the backscattered field must be evaluated for a number of time steps before the Doppler spectrum can be calculated as its Fourier transform. For a better understanding

Manuscript received May 1, 1998; revised May 21, 1999. This work was supported by the Deutsche Forschungsgemeinschaft under Contract Al 88/2, the European Community as a part of the Marine Science and Technology (MAST) program under Contract MAS3-CT95-0035, the Alexander von Humboldt Stiftung, and the U.S. Office of Naval Research.

R. Romeiser is with the Universität Hamburg, Institut für Meereskunde, 22529 Hamburg, Germany (e-mail: romeiser@ifm.uni-hamburg.de).

D. R. Thompson is with Applied Physics Laboratory, Johns Hopkins University, Laurel, MD 20723 USA (e-mail: thompson@nansen.jhuapl.edu).

Publisher Item Identifier S 0196-2892(00)00426-5.

of the analyses of the ATI imaging mechanism and for extensive numerical analyzes including the simulation of a number of ATI images, it would be desirable to have a simplified model which reduces the calculation of Doppler spectra and ATI phase differences to an evaluation of a few key expressions. For the simulation of SAR intensity images, this has been achieved with the development of composite surface models based on the simple equations of Bragg scattering theory [7], [8]. We show in this paper that a composite surface model approach can also be used for ATI simulations.

In the following section, we present the theory of the proposed model. In Section III we show by comparison with the fundamental model described in [6] that both models predict comparable Doppler spectra, while theoretical computation times can be reduced by more than one order of magnitude by using the proposed composite surface model. Finally, we discuss theoretical possibilities and limitations of oceanic current measurements by ATI in Section IV and summarize our findings in Section V.

II. THEORY OF THE MODEL

In general, the Doppler frequency f_D of the radar backscatter from a moving target is given by

$$f_D = -k_e v_r / \pi \quad (1)$$

where k_e is the magnitude of the electromagnetic wave vector and v_r the line-of-sight (radial) component of the target velocity. In our convention, a positive value of v_r , thus a negative Doppler frequency, corresponds to a target which is receding from the radar.

Since the backscattering of microwaves at the ocean surface is, for moderate incidence angles, dominated by resonant Bragg scattering [2], [3] (see also Section II-B), some Doppler shift will always result from the phase speed of the short Bragg waves at the ocean surface which are in resonance with the electromagnetic waves. If no surface currents and longer waves were present, the Doppler spectrum would consist of two lines corresponding to the (positive and negative) speed of the Bragg wave components traveling toward and away from the radar, and the intensities of the two lines would be proportional to the square amplitudes (waveheight spectral densities) of the Bragg wave components. In the presence of a mean surface current, both lines would experience an additional frequency shift in the same direction. In general, another contribution can result from the speed component of the antenna platform in range direction, but we will assume in the following that this contribution is known and can be removed from the data before further processing.

In case of a real ocean surface, the two lines of the idealized Doppler spectrum will be broadened due to the presence of orbital motions of ocean waves that are longer than the Bragg waves. A simple model for this effect was presented by Plant and Keller [9]. However, their theory does not account for the fact that correlated variations of the line-of-sight velocity and the radar backscattering cross section of ocean surface facets can result in an additional mean Doppler shift. In the following, we shall develop expressions for the Doppler spectrum which include these contributions.

A. Doppler Spectra

The variations of the Doppler frequency of a backscattered microwave signal along sinusoidal ocean waves are linear in the surface elevation (or surface slope) variations. Assuming that the modulating wave components are independent of each other, the Doppler frequency resulting from the interaction with a facet at the ocean surface at position \mathbf{x} and time t can thus be written in terms of a linear modulation transfer function (MTF)

$$f_{D\pm}(\mathbf{x}, t) = f_{D\pm}^{(0)} + \text{Re} \left\{ \iint D(\mathbf{k}) \hat{\zeta}(\mathbf{k}) e^{-i(\mathbf{k}\mathbf{x} - \omega t)} d^2k \right\} \quad (2)$$

where

D	(complex) Doppler MTF;
ζ	surface elevation;
$\hat{\zeta}$	denotes its Fourier transform;
i	imaginary unit;
$k = \mathbf{k} $ and ω	wavenumber and angular frequency of the ocean waves that modulate the Doppler frequency.

Furthermore, f_{DB} and f_{D+} denote the Doppler frequencies resulting from the scattering at Bragg waves propagating toward and away from the radar, respectively. The two quantities differ only in the zeroth-order Doppler frequencies $f_{D-}^{(0)}$ and $f_{D+}^{(0)}$ which represent the contributions associated with the phase velocities of the two Bragg wave components and with a possible mean surface current. In the absence of a mean current, $f_{D-}^{(0)}$ will be positive and $f_{D+}^{(0)}$ will be negative with the same absolute value. As shown in [10], an exact analytical expression for the Doppler MTF is

$$D(\mathbf{k}) = \frac{k_e}{\pi} \frac{\omega(\mathbf{k})}{k} \left(-\frac{k_r}{k} \sin \theta + i \cos \theta \right) \quad (3)$$

where θ is the incidence angle of the radar with respect to nadir and k_r is the component of the ocean wavenumber vector parallel to the radar look direction (range direction). The phase of $D(\mathbf{k})$ is defined such that it is zero at a wave's crest and positive in the direction determined by the wavenumber vector (i.e., the propagation direction of the wave).

As discussed in [8], the normalized radar backscattering cross section (NRCS) of the sea surface including variations up to second order in the surface slopes parallel and normal to the radar look direction can be written as

$$\begin{aligned} \sigma(\mathbf{x}, t) &= \sigma^{(0)} + \text{Re} \left\{ \iint \hat{\sigma}(\mathbf{k}) e^{-i(\mathbf{k}\mathbf{x} - \omega t)} d^2k \right\} \\ &+ \text{Re} \left\{ \iint \iint \hat{\sigma}^{\wedge}(\mathbf{k}, \mathbf{k}') e^{-i((\mathbf{k}+\mathbf{k}')\mathbf{x} - (\omega+\omega')t)} d^2k d^2k' \right\} \\ &+ \text{Re} \left\{ \iint \iint \hat{\sigma}^{\vee}(\mathbf{k}, \mathbf{k}') e^{-i((\mathbf{k}-\mathbf{k}')\mathbf{x} - (\omega-\omega')t)} d^2k d^2k' \right\} \end{aligned} \quad (4)$$

where σ denotes the local NRCS with respect to a horizontal reference plane and $\sigma^{(0)}$ its zeroth-order value for a nontilted facet in the reference plane according to Bragg scattering theory [2], [3]. Again, \wedge denotes a Fourier transform of the variations of σ

which are linear in the surface slopes parallel and normal to the radar look direction, and the symbols $\wedge\wedge$ and $\wedge\vee$ denote Fourier transforms of oscillating and nonoscillating contributions to σ of second order in the surface slopes. Explicit expressions for these Fourier transforms can be obtained from a Taylor expansion of the basic expressions of Bragg scattering theory. Each element of the sum in (4) can furthermore be subdivided into two parts associated with the two Bragg wave components, which will again be denoted by subscripts + and - where necessary.

The linearity of the Doppler frequencies $f_{D\pm}$ in the surface slope and the general assumption that all components of the ocean wave spectrum which modulate the NRCS are independent of each other result in the fact that Doppler frequency variations along a given sinusoidal wave component will be correlated only with NRCS variations along the same wave component. Accordingly, the effect of the ocean wave spectrum on the mean Doppler spectrum can be decomposed into contributions of single sinusoidal wave components. Let us consider for a moment a scenario of an isolated sinusoidal wave of finite (complex) amplitude ζ_0 , wavenumber \mathbf{k} , and angular frequency ω . According to (2), the Doppler frequency variations along this wave are given as

$$f_{D\pm}(\mathbf{x}, t) = f_{D\pm}^{(0)} + \text{Re} \left\{ D(\mathbf{k}) k \zeta_0 e^{-i(\mathbf{k}\mathbf{x} - \omega t)} \right\}. \quad (5)$$

Accounting for the fact that, according to (4), the NRCS variations along the wave can be approximated by sinusoidal oscillations of frequencies and wavenumbers ω , \mathbf{k} and 2ω , $2\mathbf{k}$, we can write

$$\sigma_{\pm}(\mathbf{x}, t) = \langle \sigma_{\pm} \rangle \left(1 + \text{Re} \left\{ M_{1\pm}(\mathbf{k}) k \zeta_0 e^{-i(\mathbf{k}\mathbf{x} - \omega t)} + M_{2\pm}(\mathbf{k}) k^2 \zeta_0^2 e^{-i2(\mathbf{k}\mathbf{x} - \omega t)} \right\} \right) \quad (6)$$

where $\langle \sigma_{\pm} \rangle$, are the expectation values (mean values) of σ_{\pm} , and $M_{1\pm}$ and $M_{2\pm}$ are linear MTF's describing the relation between first- and second-order slope and NRCS oscillations (for a discussion of the meaning of $M_{1\pm}$, see Section II-B). Again, the symbol \pm indicates that there may be differences between the NRCS contributions and the MTF's associated with the two Bragg wave components.

The Doppler spectrum can be considered as distribution of Doppler frequencies associated with standardized small elements of backscattered power. In case of the single sinusoidal wave we obtain for the first moments of the distributions associated with the two Bragg wave components

$$\begin{aligned} \langle f_{D\pm} \rangle_{\sigma} &= \frac{\langle f_{D\pm} \sigma_{\pm} \rangle}{\langle \sigma_{\pm} \rangle} = \frac{1}{2\pi} \int_0^{2\pi} \left(f_{D\pm}^{(0)} + \text{Re} \left\{ D k \zeta_0 e^{-i\alpha} \right\} \right) \\ &\cdot \left(1 + \text{Re} \left\{ M_{1\pm} k \zeta_0 e^{-i\alpha} + M_{2\pm} k^2 \zeta_0^2 e^{-i2\alpha} \right\} \right) d\alpha \\ &= f_{D\pm}^{(0)} + \frac{1}{2} \text{Re} \left\{ D^* M_{1\pm} \right\} k^2 \zeta_0^* \zeta_0 \end{aligned} \quad (7)$$

where we have substituted $\alpha = \mathbf{k}\mathbf{x} - \omega t$. Furthermore, the subscript σ of $\langle f_{D\pm} \rangle_{\sigma}$ indicates that this expectation value characterizes the mean value of a property of normalized elements of the NRCS (i.e., an NRCS-weighted mean value), while the expectation value symbol $\langle \dots \rangle$ without subscript characterizes results of conventional averaging in space and time without weighting.

In addition to $\langle f_{D\pm} \rangle_{\sigma}$ we can calculate

$$\begin{aligned} \langle f_{D\pm}^2 \rangle_{\sigma} &= \frac{\langle f_{D\pm}^2 \sigma_{\pm} \rangle}{\langle \sigma_{\pm} \rangle} = \frac{1}{2\pi} \int_0^{2\pi} \left(f_{D\pm}^{(0)} + \text{Re} \left\{ D k \zeta_0 e^{-i\alpha} \right\} \right)^2 \\ &\cdot \left(1 + \text{Re} \left\{ M_{1\pm} k \zeta_0 e^{-i\alpha} + M_{2\pm} k^2 \zeta_0^2 e^{-i2\alpha} \right\} \right) d\alpha \\ &= \left(f_{D\pm}^{(0)} \right)^2 + f_{D\pm}^{(0)} \text{Re} \left\{ D^* M_{1\pm} \right\} \\ &\cdot k^2 \zeta_0^* \zeta_0 + \frac{1}{2} D^* D k^2 \zeta_0^* \zeta_0 + O(\zeta_0^4) \end{aligned} \quad (8)$$

where the contributions of fourth order in the wave's amplitude ζ_0 will not be used in the following for consistency reasons. Neglecting contributions beyond second order once more, we obtain from (7) and (8) an expression for the variances of the two parts of the "elementary" Doppler spectrum associated with a sinusoidal wave of amplitude ζ_0

$$\langle f_{D\pm}^2 \rangle_{\sigma} - \langle f_{D\pm} \rangle_{\sigma}^2 = \frac{1}{2} D^* D k^2 \zeta_0^* \zeta_0. \quad (9)$$

Note that this expression is independent of NRCS variations, so that both parts of the Doppler spectrum have exactly the same variance (or bandwidth) in this approximation.

Switching back to the scenario of a complete ocean wave spectrum, we can now take advantage of the fact that, according to (2) and (4), the total Doppler variations as well as the correlated NRCS variations can be written as integrals of the contributions of single wave components. According to the central limit theorem, the distributions of the two total Doppler frequencies $f_{D\pm}$ as sums of large numbers of independent contributions must be Gaussian distributions. Furthermore, the mean value and the variance of a quantity which is a sum of many independent small contributions are equal to the sums of the mean values and of the variances of the individual contributions. Replacing finite amplitudes in (7) and (9) by differential amplitudes and integrating over the wave spectrum, we obtain thus for the parameters of the total Doppler spectrum

$$\langle f_{D\pm} \rangle_{\sigma} = f_{D\pm}^{(0)} + \text{Re} \left\{ \iint D^*(\mathbf{k}) M_{1\pm}(\mathbf{k}) k^2 \Psi(\mathbf{k}) d^2 k \right\} \quad (10)$$

and

$$\gamma_{D\pm}^2 \equiv \langle f_{D\pm}^2 \rangle_{\sigma} - \langle f_{D\pm} \rangle_{\sigma}^2 = \iint D^*(\mathbf{k}) D(\mathbf{k}) k^2 \Psi(\mathbf{k}) d^2 k \quad (11)$$

where Ψ denotes the waveheight spectrum defined by

$$\Psi(\mathbf{k}) \delta(\mathbf{k} - \mathbf{k}') = \frac{1}{2} \langle \hat{\zeta}^*(\mathbf{k}') \hat{\zeta}(\mathbf{k}) \rangle \quad (12)$$

Furthermore, δ denotes the Dirac delta distribution, and we use γ^2 as symbol for a variance. The integrations in (10) and (11) run over all directions and over wavenumbers up to $1/6$ of the Bragg wavenumber, as discussed in the paper [8] on NRCS model calculations.

Using the mean values and variances given by (10) and (11) and normalizing the two components of the Doppler spectrum such that their integrals yield the expectation values of the corresponding NRCS components according to (4), we finally obtain for the Doppler spectrum

$$\begin{aligned} S(f_D) &= \frac{\langle \sigma_{+} \rangle}{\sqrt{2\pi\gamma_{D+}^2}} e^{(f_D - \langle f_{D+} \rangle_{\sigma})^2 / \gamma_{D+}^2} \\ &+ \frac{\langle \sigma_{-} \rangle}{\sqrt{2\pi\gamma_{D-}^2}} e^{(f_D - \langle f_{D-} \rangle_{\sigma})^2 / \gamma_{D-}^2} \end{aligned} \quad (13)$$

B. NRCS Mean Values and Variations

Expressions for the expectation values $\langle \sigma_{\pm} \rangle$ of the NRCS contributions associated with the two Bragg wave components are given in [8] and do not need to be derived again in this work. However, we would like to give a brief overview of the terms of the NRCS and the meaning of the MTF's $M_{1\pm}$ in (10) and their implementation in our numerical model.

Understanding the NRCS of a facet of the ocean surface as radar backscattering cross section normalized with respect to a horizontal standard area at nominal sea level, we can combine the expressions given in [3] and in [8] to obtain

$$\sigma = w(H, \zeta, s_p, s_n) T(f_e, \theta, s_p, s_n) (\Psi(\mathbf{k}_B) + \Psi(-\mathbf{k}_B)) \quad (14)$$

where the function w accounts for variations of the geometric cross section of the facet as seen from the radar with facet elevation ζ and slopes s_p and s_n in the directions parallel and normal to the radar look direction, respectively, H is the vertical distance between the radar antenna and $\zeta = 0$, and T is a proportionality factor derived from fundamental electrodynamic expressions. Explicit expressions for T and for w can be found in [3] and [8], respectively. Furthermore, \mathbf{k}_B in (14) is the Bragg wavenumber, and f_e and θ are the radar frequency and nominal incidence angle. In this context we would like to mention that the validity of expression (14) and thus the validity of the entire proposed model in its present form is limited to moderate incidence angles θ between, say, 30° and 60° . At incidence angles outside this range, contributions from additional scattering mechanisms, such as specular reflection at very steep incidence angles, must be taken into account.

As shown in [8], an expectation value of the NRCS can be calculated by using the decomposition of $\sigma(\mathbf{x}t)$ according to (4), replacing Fourier transforms of first- and second-order variations of σ by corresponding elements of a Taylor expansion, and averaging in space and time. Only nonoscillating contributions of zeroth and second order in the surface slope, i.e., the first and the last term in (4), survive this procedure, yielding an expression of the form

$$\langle \sigma \rangle = \sigma^{(0)} + \langle \sigma^{(2)} \rangle \quad (15)$$

where $\sigma^{(0)}$ is an unperturbed zeroth-order term as obtained from (14) for vanishing slopes s_p and s_n and elevation ζ , and $\langle \sigma^{(2)} \rangle$ represents a sum of second-order terms which depend on the mean square surface slopes parallel and normal to the radar look direction. All terms are proportional to the waveheight spectral density of the Bragg waves. At horizontal transmit/receive (HH) and vertical transmit/receive (VV) polarization of the radar, the relative contribution of $\langle \sigma^{(2)} \rangle$ increases with wind speed and radar frequency and is clearly larger at HH than at VV. At HH, $\langle \sigma^{(2)} \rangle$ can be even larger than $\sigma^{(0)}$ [11]. At cross polarization (horizontal transmit/vertical receive, HV, or vice versa, VH), the factor T in (14) vanishes for an untilted Bragg scattering facet, so that $\langle \sigma^{(2)} \rangle$ is the lowest-order contribution and thus the only contribution to the NRCS at HV or VH in the proposed model.

According to (10), the Doppler offsets $\langle f_{D\pm} \rangle$ depend on the two linear MTF's $M_{1\pm}$ which describe zero-mean oscillations of the expectation value of the NRCS which are linear in the

slopes of the modulating waves. The definition given by (6) suggests that these MTF's should be given by

$$M_{1\pm}(\mathbf{k}) = -\frac{i}{k} \frac{1}{\langle \sigma_{\pm} \rangle} \left. \frac{\partial \hat{\sigma}_{\pm}}{\partial \hat{\zeta}} \right|_{\hat{\zeta}=0} \quad (16)$$

where we use $\hat{\sigma}_{\pm}(\mathbf{k})$ as symbol for the Fourier transforms of linear variations of the sums of zeroth- and ensemble-averaged second-order terms of the NRCS with the local slope of a particular modulating wave of wavenumber \mathbf{k} . That is, $M_{1\pm}$ describes not only the first-order variations of σ_{\pm} , but it includes the effect of variations of second-order terms which are correlated with the slope of a modulating wave. Analytical exact expressions for $M_{1\pm}$ would be quite complex. A numerical computation is feasible but time-consuming; a possible approach is described in [12]. However, since we expect only minor corrections but enormous computational efforts from an inclusion of linear second-order term variations in $M_{1\pm}$, we use the approximation

$$M_{1\pm}(\mathbf{k}) = -\frac{i}{k} \frac{1}{\langle \sigma_{\pm} \rangle} \left. \frac{\partial \hat{\sigma}_{\pm}}{\partial \hat{\zeta}} \right|_{\hat{\zeta}=0} \approx -\frac{i}{k} \frac{1}{\sigma_{\pm}^{(0)}} \left. \frac{\partial \hat{\sigma}_{\pm}}{\partial \hat{\zeta}} \right|_{\hat{\zeta}=0} \quad (17)$$

i.e., we neglect contributions of second-order terms of the NRCS to both the mean value and the variations along the modulating wave. The remaining analytical expressions for $M_{1\pm}$ account for the following effects:

- 1) Variations of the local incidence angle along waves that are long compared to the Bragg scattering facets modulate the factor T and the Bragg wavenumber vector k_B in (14). The part of $M_{1\pm}$ that describes this effect is usually called the tilt MTF [13].
- 2) In addition to this, variations of facet slope and elevation enter into the weighting function w , resulting in another "geometric" contribution to the MTF [12], which is sometimes called the range MTF.
- 3) Another contribution, which is responsible for differences between M_{1-} and M_{1+} , is the "hydrodynamic" MTF, $M_{h\pm}$. It describes the variations of the Bragg wave intensities along longer waves due to hydrodynamic interaction, i.e., the variations of $\Psi(\mathbf{k}_B)$ and $\Psi(-\mathbf{k}_B)$ with s_p and s_n . An analytical expression for the hydrodynamic MTF was derived by Alpers and Hasselmann [14]; a slightly modified version can be found in [8]. Since both versions were misprinted, we would like to take this opportunity to clarify that the correct form should read

$$M_{h\pm} = - \left(\cos^2 \Delta\Phi_{\pm} \left(\frac{k}{\Psi(\mathbf{k}_{B\pm})} \frac{\partial \Psi}{\partial k} \Big|_{\mathbf{k}=\mathbf{k}_{B\pm}} - \eta \right) + \cos \Delta\Phi_{\pm} \sin \Delta\Phi_{\pm} \frac{1}{\Psi(\mathbf{k}_{B\pm})} \frac{\partial \Psi}{\partial \Phi} \Big|_{\mathbf{k}=\mathbf{k}_{B\pm}} \right) \cdot \frac{\Omega^2 + i\mu_{\pm}\Omega}{\Omega^2 + \mu_{\pm}^2} \quad (18)$$

where

- $\Delta\Phi$ direction of the modulating wave with respect to the Bragg wave;
- Ω ratio between group velocity and phase velocity of the Bragg wave;
- Ω angular frequency of the modulating wave;

μ relaxation rate of the Bragg wave, which depends on wavenumber, wave direction, and wind speed.

The two-dimensional (2-D) version of $M_{h\pm}$, which is used in [8], can be written as follows:

$$\begin{aligned} M_{h\pm}^p &= |\cos \Phi| \operatorname{Re} M_{h\pm} + \cos \Phi \operatorname{Im} M_{h\pm} \\ M_{h\pm}^n &= |\sin \Phi| \operatorname{Re} M_{h\pm} + \sin \Phi \operatorname{Im} M_{h\pm} \end{aligned} \quad (19)$$

where Φ is the direction of the modulating wave with respect to the radar look direction and superscripts p and n denote components of the 2-D hydrodynamic MTF which are associated with wave slopes parallel and normal to the radar look direction.

We end up with the following expression for $M_{1\pm}$:

$$\begin{aligned} M_{1\pm}(k, \Phi) &= -\frac{i}{k} \frac{1}{\langle \sigma^{(0)} \rangle} \left. \frac{\partial \hat{\sigma}}{\partial \hat{\zeta}} \right|_{\hat{\zeta}=0} = -\frac{i}{k} \left(\frac{1}{w_0} \left. \frac{\partial \hat{w}}{\partial \hat{\zeta}} \right|_{\hat{\zeta}=0} \right. \\ &\quad \left. + \frac{1}{T_0} \left. \frac{\partial \hat{T}}{\partial \hat{\zeta}} \right|_{\hat{\zeta}=0} \right. \\ &\quad \left. + \frac{1}{\Psi(\mathbf{k}_{B\pm})} \left. \frac{\partial \Psi}{\partial \mathbf{k}} \right|_{\mathbf{k}=\pm \mathbf{k}_B} \left. \frac{\partial \hat{\mathbf{k}}_B}{\partial \hat{\zeta}} \right|_{\hat{\zeta}=0} \right) + M_{h\pm} \end{aligned} \quad (20)$$

where w_0 and T_0 are unperturbed zeroth-order quantities. One could argue that this expression has a singularity at cross polarization, where $T_0 = 0$, but in fact also $\partial \hat{T} / \partial \hat{\zeta}$ will be 0 in that case, and one can show that M_T vanishes. Accordingly, the proposed model can be used very well for calculations for HH, VV, and HV/VH polarization.

C. SAR/ATI Intensity and Phase Images

Synthetic aperture radar (SAR) images are generally distorted by an azimuthal displacement effect resulting from a misinterpretation of the phase history of the radar backscatter from moving targets [15]–[17]. ATI phase images are also affected by this distortion. One can easily show that the apparent location of a moving target in a SAR image is displaced from the actual location in azimuth direction by the amount

$$\Delta x = -\frac{R}{V} v_r = \frac{R}{V} \frac{\pi}{k_e} f_D \quad (21)$$

where R is the distance between radar antenna and target, and V is the velocity component of the SAR platform in azimuth (x) direction. The azimuthal shift is directed such that targets moving toward the radar are displaced in flight direction and targets receding from the radar are displaced against the flight direction.

A SAR image of the ocean surface can be simulated by computing the Doppler spectrum for each cell of a surface grid and mapping elements of the backscattered power to image pixels according to (21), using the distribution of Doppler frequencies given by the Doppler spectrum. The mean Doppler frequency and the bandwidth obtained for a grid cell correspond to a mean azimuthal displacement and blurring, respectively, of the pixel intensity in the simulated image. Where only radar signatures of stationary features are considered, the contributions of surface waves to Doppler offsets and bandwidths in (10) and (11) and to $\langle \sigma_{\pm} \rangle$ as given explicitly in [8] must be

integrated over all wavenumbers up to the cutoff wavenumber, which is $1/6 k_B$ in the proposed model [8]. This corresponds to averaging of all statistically varying and nonstationary contributions. For the simulation of radar signatures of ocean surface waves, on the other hand, the Doppler integrations must cover only subresolution-scale waves, while surface slopes, elevations, and orbital velocities of longer waves must be treated deterministically. Furthermore, artifacts resulting from nonsynoptic imaging at finite platform speeds, like apparent changes of wavenumbers and wave directions in radar images [18], must be taken into account. In the present paper however, only radar signatures of quasistationary surface current variations will be discussed.

The processing of received raw data from a SAR system will first result in a complex (amplitude) image (for an illustration of the SAR processing technique, see [19]). The phase obtained for a pixel of a complex image does normally not provide useful information, since it results from interference of many small contributions to the backscattered signal with different phases and has thus a random distribution. However, the evolution of the phase of the backscattered signal with respect to a reference signal will be deterministic within a finite decorrelation time interval. Both the phase change and the decorrelation time are determined by the Doppler spectrum. As shown in [5], the expectation value of the phase change within a time lag τ is equal to the phase of the autocorrelation of the backscattered field for this time interval, $R_P(\tau)$, which is related to the Doppler spectrum by

$$R_P(\tau) = \frac{1}{\langle \sigma \rangle} \int_{-\infty}^{\infty} e^{i2\pi f_D \tau} S_P(f_D) df_D \quad (22)$$

where $S_P(f_D)$ denotes the Doppler spectrum associated with an actual pixel of the SAR image—in contrast to $S(f_D)$ as given by (13), which is the Doppler spectrum of a model grid cell with the local wave spectrum Ψ before accounting for azimuthal displacement effects. Pixel-related Doppler spectra can be computed from grid-point related ones by mapping power elements from all cells of a model grid into pixels according to (21) and keeping their frequency information.

If $1/\tau$ is large compared to the bandwidth of the Doppler spectrum, the phase of $R_P(\tau)$ can be approximated by

$$\arg(R_P(\tau)) = \frac{2\pi\tau}{\langle \sigma \rangle} \int_{-\infty}^{\infty} f_D S_P(f_D) df_D \quad (23)$$

i.e., by an expression which is proportional to the first moment of the Doppler spectrum (except for an ambiguity of multiples of 2π which must be removed by phase unwrapping techniques in practical applications). If $1/\tau$ is comparable to or smaller than the Doppler bandwidth, on the other hand, the magnitude of $R_P(\tau)$ becomes very small, indicating that the backscattered field decorrelates within the time lag τ such that $\arg(R_P(\tau))$ is practically meaningless. In our numerical model, magnitude and phase of $R_P(\tau)$ are computed exactly, i.e., approximation (23) is not used. In the context of this work we use it only to illustrate the meaning of phase differences between SAR images.

Despite the fact that each pixel in a SAR image is composed of contributions to the backscattered signal with a well-defined phase history and that the Doppler shift information is converted into an azimuthal displacement and virtually lost during data

processing, phase changes according to (22) or (23) can be detected if the received signal is sampled and processed a second time after a short time lag τ within the decorrelation time interval. The along-track interferometric SAR technique is based on this principle, using two receiving antennas which are separated by some distance in flight direction. Accordingly, an ATI system can measure Doppler offsets, which represent, as discussed in Section II-A, a power-weighted mean value of the Doppler frequencies resulting from the line-of-sight velocities of the scatterers. To simulate ATI phase images, we construct the Doppler spectrum associated with each single pixel of a SAR image as described above, and we compute the corresponding phase of $R_P(\tau)$.

III. MODEL VALIDATION

As already mentioned, the scattering model described in [6] is known from previous studies to explain measured Doppler spectra and ATI signatures quite well [4]–[6], [20] (note that the model validation in [6] was based on L and K_u band data by Plant and Keller which were later published in [9]). This model is based explicitly on Maxwell's equations. For the computation of a Doppler spectrum, the field autocorrelation function of a moving ocean surface is computed, and the Doppler spectrum is obtained as the Fourier transform of this function. Depending on parameters like radar frequency and wind speed, as many as 100 time steps, i.e., 100 integrations of the backscattered field, can be required for the computation of a full Doppler spectrum [nevertheless, a few time steps are usually sufficient for the estimation of the mean Doppler frequency alone, which allows to estimate an ATI phase difference according to (23)].

In contrast to this, the model proposed in this work does not require explicit time-dependent calculations. All parameters of the Doppler spectrum, including modulus and phase of the autocorrelation function of the field for a given ATI time lag, can be integrated within one loop of numerical code. The computation efforts are comparable to those required for one single time step in the fundamental model. Accordingly, a reduction of computation times by a factor of up to 100 can be expected. On the other hand, it is not obvious that both models can be considered equivalent in the sense that they produce the same results.

In order to validate the proposed model, we have computed Doppler spectra for some scenarios with both models, considering the fundamental model as reference. While calculations with the proposed model are usually done with the parameterization of the wave spectrum proposed in [8], the Bjerkaas-Riedel spectrum [21] was consistently used in both models for this comparison. Nevertheless, one should be aware of the fact that the proposed model in its present form does not account for specular reflection while, on the other hand, hydrodynamic modulation of the Bragg waves by longer waves is not included in the fundamental model. Small deviations between the predictions of the two models should thus be expected.

Fig. 1 shows simulated Doppler spectra for L band (1.0 GHz), VV polarization, an incidence angle of 30° , a radar look direction of 75° with respect to the downwind direction, and wind speeds of 3, 6, and 12 m/s. There is no

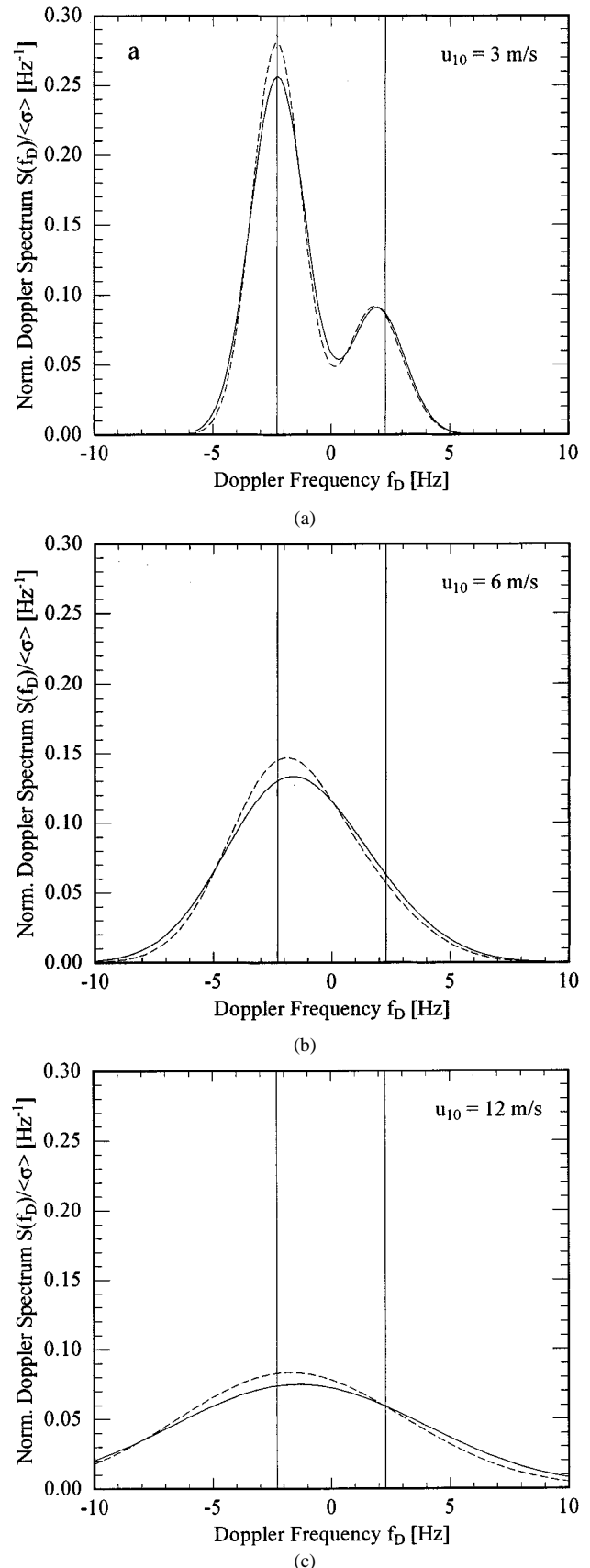


Fig. 1. Simulated normalized Doppler spectra as obtained from the proposed composite surface model (solid lines) and from the fundamental model described in [6] (dashed lines) for L band (1.0 GHz), vertical (VV) polarization, an incidence angle of 30° , and a radar look direction of 75° with respect to the wind direction, and for the wind speeds: (a) 3 m/s; (b) 6 m/s; and (c) 12 m/s.

mean surface current in these examples. In order to eliminate the effect of different absolute NRCS levels in the two models and at the different wind speeds, all spectra have been normalized such that their integrals yield 1. The figure shows that both models predict Doppler spectra of similar shapes and with comparable bandwidths and Doppler offsets. In particular, both models show two separate peaks for the two Bragg wave components in the 3 m/s case, which are broadened with increasing wind speed until a quasi-Gaussian spectrum is obtained in the 12 m/s case. Similar agreement is also found for other radar parameters, which indicates that the dominant mechanisms that are responsible for the shape of Doppler spectra at moderate incidence angles are well preserved in the proposed model despite all simplifications.

As expected, clear differences between both models are found in the required computation times. It is difficult to quantify the advantage of the proposed model in this discipline on the basis of actual CPU times, since both models are implemented on completely different platforms. Furthermore, the fundamental model has not been optimized at all for computation time efficiency. However, as discussed above, the proposed Doppler model should be about 10–100 times faster than the fundamental model, since it does not require time-dependent integrations. On a 450 MHz Pentium-II computer, the computation of a set of 200×200 pixel ATI images (intensity, phase, and autocorrelation) with the proposed model (using existing spatially varying wave spectra) takes only about 3 min, which is much more convenient for practical applications than computation times of the fundamental model on the order of some hours to days (on a comparable platform). Short computation times are particularly useful where ATI simulations need to be carried out several times to optimize an estimated current field iteratively until simulated and measured ATI signatures agree.

IV. POSSIBILITIES AND LIMITATIONS OF ATI CURRENT MEASUREMENTS

To assess theoretical possibilities and limitations of current measurements by ATI, we have generated two simple test current fields and computed the corresponding modulation of the surface wave spectrum according to weak hydrodynamic interaction theory, using the method described in [11]. The two current fields are characterized by: 1) a current in x direction which changes linearly from 0.8 to 1.0 m/s within 50 m, stays constant for 300 m, and returns to a value of 0.8 m/s within another 50 m and 2) a current in y direction which changes linearly from 0.0 to 0.2 m/s within 50 m in x direction. The first current field and a divergence followed by a convergence, with a mean current on the order of 1 m/s, resembles a tidal current modulated by an underwater sandwave; the second one with a spatially limited current shear resembles an oceanic front. Spatially varying wave spectra were computed for wind speeds of 5 and 10 m/s and for wind directions toward 0° (x direction), 45° , 90° (y direction), 135° , and 180° . To investigate the dependence of ATI signatures on radar frequency, incidence angle, and polarization, Doppler spectra were then computed for L band (1.0 GHz) and X band (10.0 GHz), incidence angles of 30 and 60° , HH and

VV polarization, and for radar look directions down the x axis and down the y axis.

A. Dependence of ATI Signatures on Radar Frequency, Polarization, and Incidence Angle

As discussed in Section II, the phase difference measured by an ATI system is, for sufficiently short time lags τ and except for an ambiguity of multiples of 2π , proportional to the first moment of the Doppler spectrum [see (23)]. Postponing SAR artifacts and decorrelation and ambiguity problems to a later stage of the discussion, we will first of all discuss “Doppler velocities,” i.e., horizontal velocities whose line-of-sight projection is the radial velocity corresponding to the mean Doppler frequencies at the original model grid points. The Doppler velocities are apparent current components which would be obtained as statistical mean values from ATI measurements in the absence of artifacts of the SAR imaging technique.

Figs. 2–4 show examples of simulated Doppler velocity signatures for the convergent current (Figs. 2 and 3) and for the shear current (Fig. 4). Only results for VV polarization are shown, since the simulated velocity signatures for HH exhibit very similar behavior, except for somewhat larger absolute phase differences and more pronounced distortions of the signatures which result from larger relative contributions of longer waves. Together with the fact that the NRCS of the ocean surface and thus the achievable signal-to-noise ratio is clearly larger at VV than at HH, the finding that the relation between Doppler velocities and actual surface currents should be more linear at VV than at HH suggests that VV polarization is clearly favorable for current measurements.

Each pair of plots in Figs. 2–4 shows the x and y components of the actual surface current as bold lines and the Doppler velocities for the two corresponding radar look directions as narrow lines, using different line styles for different wind directions. Ideally, one would like to have as little offset between the actual and ATI-derived velocity components and, even more important, as little differences in the shapes of their spatial variations as possible. Furthermore, the ATI signatures should depend as little as possible on wind speed and direction, since these parameters are often not well known.

Figs. 2 and 3 show that the mapping of surface currents into Doppler velocities is much more linear at high incidence angles like 60° than at the relatively steep incidence angle of 30° . This can be explained by the fact that the relative contribution of vertical wave motions decreases with increasing incidence angle, while the contribution from the line-of-sight component of the horizontal current increases. The intensity of wave motions, i.e., the wave intensity, varies with the current gradient rather than with the current itself. Furthermore, a pronounced variation of the mean Doppler velocity with the wind direction is found. This effect results from the different intensities of the two Bragg wave components traveling toward and away from the radar at different wind directions. At the incidence angle of 60° , it is generally smaller at X band than at L band. The range of Doppler velocity variations with the wind direction increases with the wind speed, but the increase is very small at X band

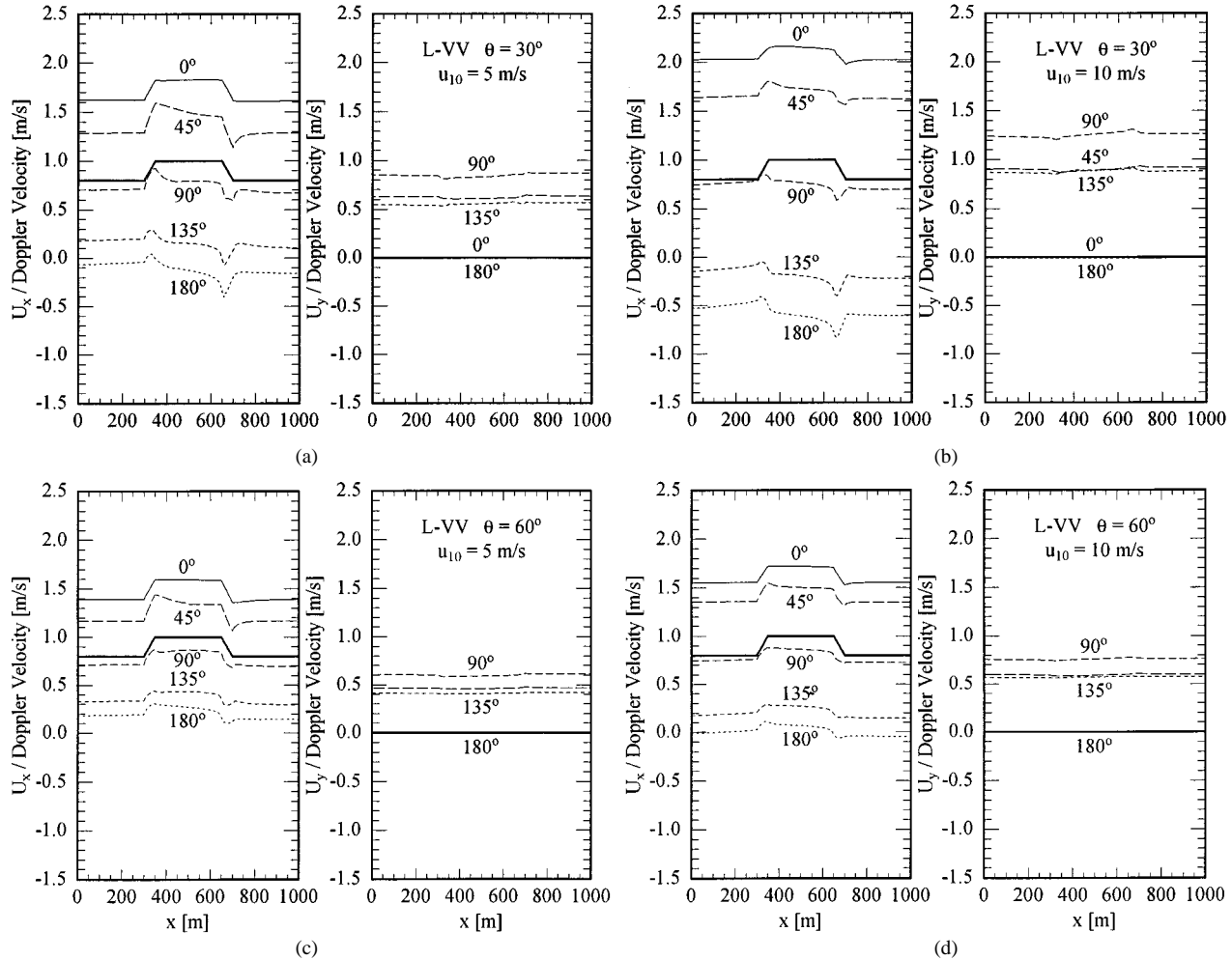


Fig. 2. Simulated Doppler velocity signatures of a simple divergent/convergent current feature (bold lines) for an L band (1.0 GHz) radar at VV polarization looking down the x axis (left part of plots) and looking down the y axis (right part), and for different wind directions as indicated by numbers ("toward" directions) and line styles; incidence angles and wind speeds are: (a) 30° and 5 m/s; (b) 30° and 10 m/s; (c) 60° and 5 m/s; and (d) 60° and 10 m/s.

and 60° . The linearity between actual currents and Doppler velocities at this incidence angle is better at a wind speed of 10 m/s than at 5 m/s.

While a clear superiority of high or low radar frequencies in terms of linearity of the imaging mechanism is not obvious from the results for the divergence/convergence scenario, Fig. 4 shows that X band appears to be better suited in case of the shear current. Fig. 4(a) shows model results for L band, VV polarization, an incidence angle of 60° , and a wind speed of 10 m/s; Fig. 4(c) shows corresponding X band results. In the latter case, the imaging mechanism is more linear. Again, also the variation of the mean Doppler velocity with the wind direction is smaller at X band. For comparison, Fig. 4(b) shows results for X band and the incidence angle of 30° , which are clearly distorted, like in the convergence/divergence cases of Figs. 2 and 3. In general, the dependencies of the simulated Doppler velocity signatures of divergent, convergent, and shear currents on the considered radar parameters and environmental parameters are very similar, thus we show only these three examples of shear current results.

Nonlinearities in L and X band Doppler velocity signatures result from intensity variations of surface waves due to hydrodynamic modulation, but the modulation mechanisms at low and high radar frequencies are different in detail. Fig. 5(a) shows

that the spatial intensity variations of the two L band Bragg wave components in the shear current scenario are quite different, which results in pronounced variations of the height of the two Gaussian parts of the Doppler spectrum with respect to each other and corresponding variations of the mean Doppler frequency. In contrast, the ratio between the intensities of the two X band Bragg wave components, as shown in Fig. 5(b), is almost constant. In general the hydrodynamic modulation of Bragg waves decreases with decreasing wavelength (i.e., with increasing radar frequency), because short waves have larger relaxation rates. The intensity change of receding Bragg waves in Fig. 5(b) results from a change of the effective wind vector rather than from hydrodynamic modulation. Nonlinearities in simulated X band signatures result mainly from intensity variations of longer waves and the corresponding spatially varying hydrodynamic modulation of the X band Bragg waves by the longer waves.

B. Motion-Induced Distortion

As discussed in Section II-C, ATI images are distorted by a motion-induced displacement in azimuth direction of targets with a velocity component in range direction. According to (21),

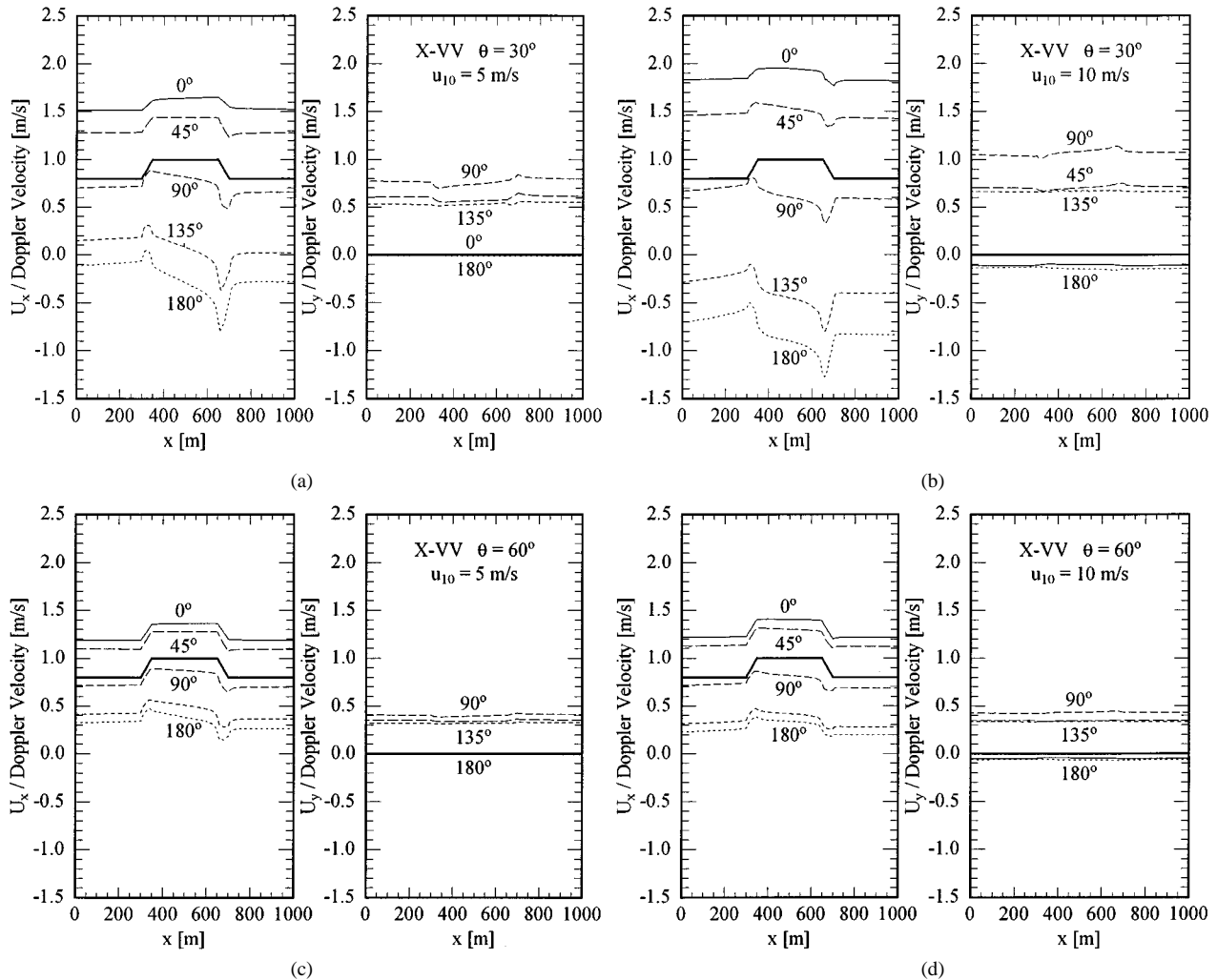


Fig. 3. Same as Fig. 2, but for X band (10.0 GHz).

the displacement is proportional to the ratio of the distance between radar antenna and target and the platform velocity, R/V , and to the Doppler offset resulting from the target's velocity. Especially signatures of shear currents as shown in Fig. 4 can be distorted significantly in ATI phase images, since the velocity in range direction and thus the azimuthal displacement of targets changes along the azimuth direction. In order to get an impression of the magnitude of this effect, we have calculated the actual phase signatures of the shear current for the conditions which appear to be optimum conditions for ATI measurements, i.e., for X band, VV polarization, and an incidence angle of 60° . Fig. 6 shows simulated ATI velocities (i.e., velocities obtained from ATI phase signatures) for a wind of 5 m/s. The bold solid line shows the actual current, the thin solid line shows the Doppler velocity as obtained without considering SAR effects. The Doppler velocity signature would be directly detected by an ATI system with R/V close to 0, i.e., with a very low flight altitude and high speed. Black and white triangles show ATI velocities obtained with an R/V ratio of 60 s, corresponding to a typical small aircraft flying at an altitude of 3000 m and a speed of 100 m/s, where black triangles correspond to a flight direction to the right and white ones to a flight direction to the left (with a look direction into the positive y direction in both cases).

Black and white circles show corresponding results for an R/V ratio of 160 s; a value corresponding to a spaceborne radar at a height of 800 km and a speed of about 7 km/s, looking at the sea surface at an incidence angle of about 45° (a typical upper limit of existing and future spaceborne wide-swath SAR's like Radarsat SAR and Envisat SAR).

While the simulated airborne ATI velocity signatures look like smoothed versions of the Doppler velocity signature which basically preserve the shape and location of the surface current feature, nonlinearities in the spaceborne ATI results are so strong that two areas of pronounced current shear show up instead of the original single area. The blurring of the signatures results from the mapping of elements of backscattered power from each grid cell into different pixels according to the shape of the Doppler spectrum, and the azimuthal offset results from nonzero-mean radial velocities. The "plateau" in the signatures for $R/V = 160$ s results from the fact that power elements from each grid cell are mapped into an azimuthal area which is wide compared to the current shear feature, and the mapping takes place in such a way that the ATI phase in the vicinity of the feature is dominated by the mean value of phases on both sides rather than by the rapidly changing local Doppler velocity. This is a good example of the possible complexity of

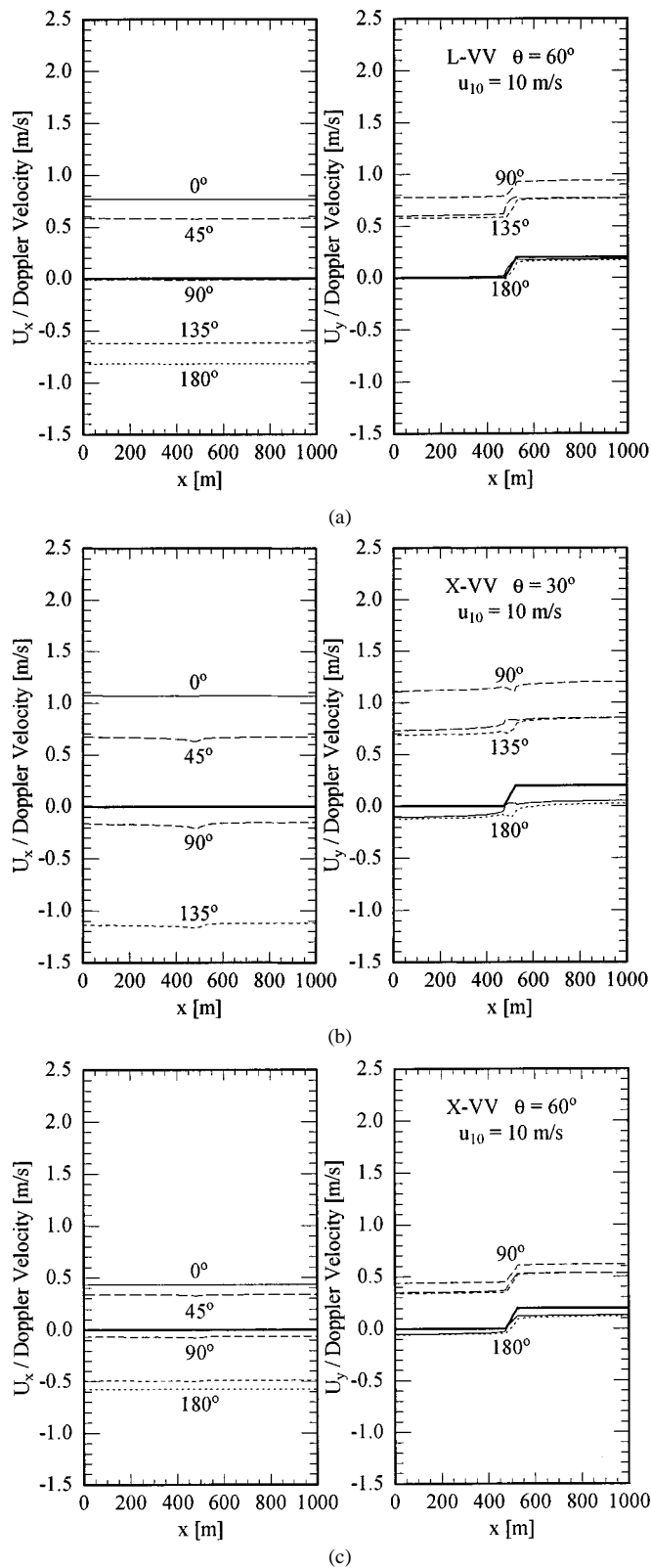


Fig. 4. Simulated Doppler velocity signatures of a simple shear current feature (current in y direction varying in x direction), presented in the same way as the signatures in Figs. 2 and 3: (a) L band, VV polarization, incidence angle = 60° , (b) X band, VV, 30° ; (c) X band, VV, 60° . Wind speed is 10 m/s.

the SAR/ATI imaging mechanism. At least in cases with large R/V ratios, phase images cannot easily be inverted into surface current fields without accounting for nonlinearities.

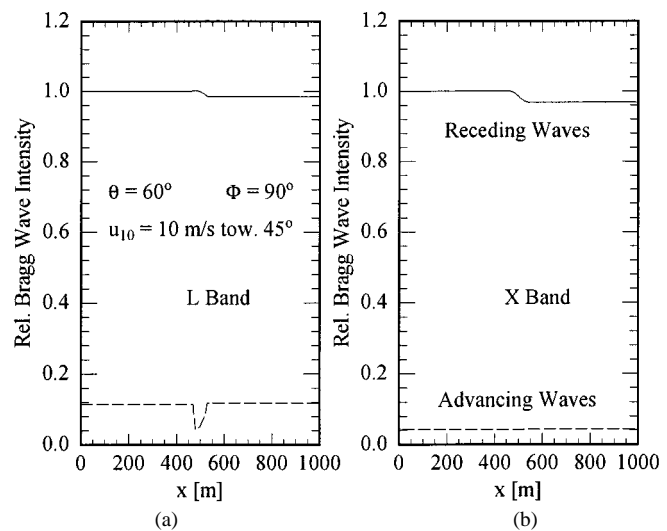


Fig. 5. Spatially varying intensities of Bragg waves advancing toward the radar (dashed lines) and receding from the radar (solid lines) for the scenario characterized in the caption of Fig. 4; all intensities are normalized by the unperturbed intensity of the receding Bragg waves at the left-hand boundary of the model grid: (a) L band Bragg waves and (b) X band Bragg waves.

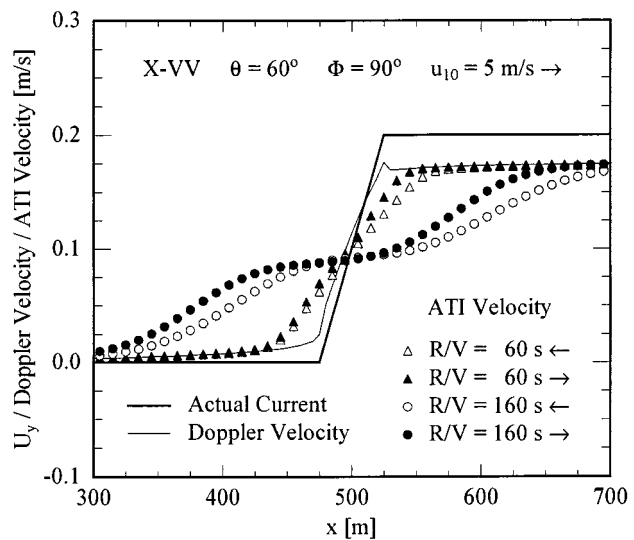


Fig. 6. Given current in y direction and simulated Doppler velocity and ATI velocity signatures of the shear current of Fig. 4 for a wind of 5 m/s blowing down the x axis, a radar frequency of 10 GHz (X band), an incidence angle of 60° , a look direction down the y axis, and an ATI time lag of 5 ms. ATI velocities are shown for R/V ratios 60 and 160 s and for flight directions to the right and to the left as indicated by arrows.

C. How to Choose the ATI Time Lag

Not only classical radar parameters like the radar frequency, polarization, and incidence angle, but also the time lag τ between the acquisition of the two complex SAR images needs to be properly chosen for successful ATI measurements. The time lag is determined by the distance d between the two receiving antennas, the platform velocity V , and the ATI mode: If both antennas are used for transmitting and receiving of separate signals, the time lag is d/V , while it is $d/2V$ if both antennas are used as receiving antennas for a signal originating from one of the antennas [22].

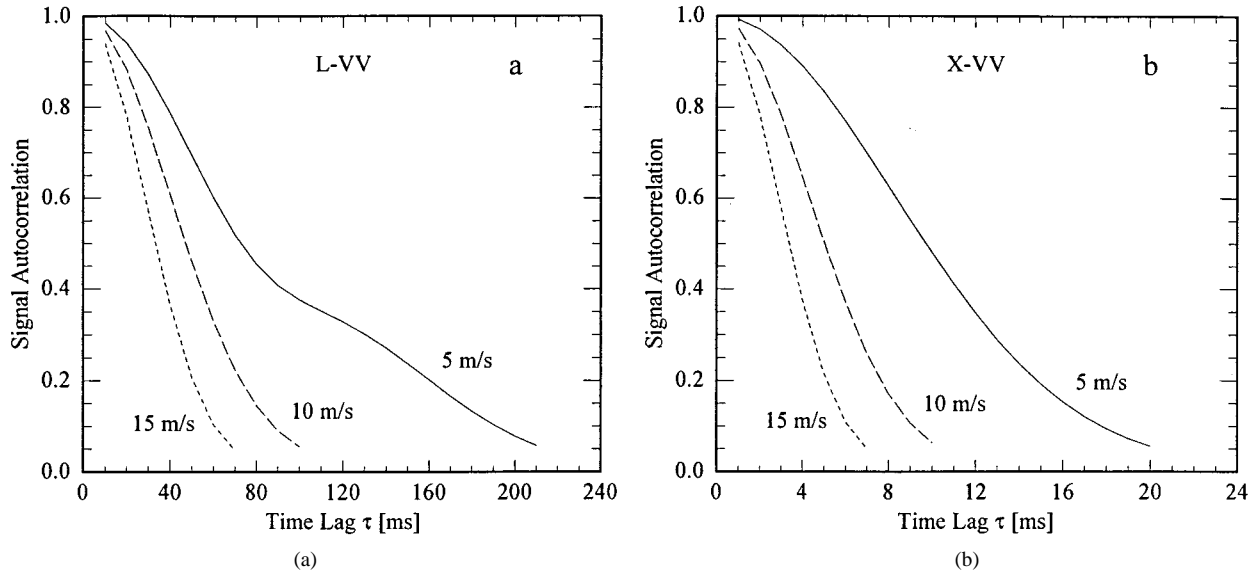


Fig. 7. Theoretical autocorrelation of the backscattered field as function of ATI time lag and for different wind speeds; radar look direction is 45° off the downwind direction; incidence angle is 60° : (a) L band VV and (b) X band, VV.

As mentioned in Section II-C, the time lag needs to be short compared to the decorrelation time of the backscattered field, which is determined by the Doppler bandwidth. Calculated autocorrelation functions for L and X band, VV, a look direction 45° off the downwind direction, and an incidence angle of 60° are shown in Fig. 7. Assuming that the autocorrelation should not be smaller than about 0.5 and that typical wind speeds during ATI measurements may be 10 m/s or less, the figure suggests that the time lag should not exceed about 50 ms at L band and 5 ms at X band.

The decorrelation times obtained from our calculations are somewhat shorter than measured values from the SAXON-FPN experiment as reported in [23] (8–10 ms at X band for a footprint size of 40 m^2). This might give rise to the impression that the model is not realistic. However, the difference can very likely be explained as a result of averaging over different footprint sizes (about 2.5 through 40 m^2 in the experiment, infinite in the model calculations), differences in the wave spectra encountered at the test site and used in the model, differences in radar look directions with respect to the wind direction, and differences in definitions and calculation methods. The decrease of decorrelation times with increasing footprint size is depicted nicely by [23, Fig. 14], which indicates X band decorrelation times of about 12–15 ms at about 2.5 m^2 and about 8–10 ms at 40 m^2 . It can be explained by the fact that the motions of scatterers within a small footprint are better correlated due to the absence of nondeterministic long wave motions. In our model this corresponds to an integration over waves that are shorter than a given footprint size. One would obtain reduced Doppler bandwidths and thus increased decorrelation times. The time lag recommendations given above appear to be reasonable for all radar look directions with respect to the wind direction \bar{B} calculated decorrelation times tend to be about 30% longer for a crosswind looking radar than for upwind or downwind look directions \bar{B} and for a wide range of incidence angles \bar{B} decorrelation times tend to decrease slightly with the incidence angle. Aside from such findings, Fig. 7 suggests that ATI measure-

ments should preferably be done at wind speeds below, say, 10 m/s in order to avoid very fast decorrelation of the backscattered field.

On the other hand, the time lag should be sufficiently long to allow for a clear modulation of the ATI phase differences by the expected surface current variations. From (23) and (1) one obtains for the conversion factor that relates ATI phases to ATI velocities

$$\frac{\Delta v_{\text{ATI}}}{\Delta \phi} = \frac{c}{720 f_e \sin \theta \tau} \left[\frac{\text{ms}^{-1}}{\text{deg}} \right] \quad (24)$$

where c is the speed of light and f_e is the nominal radar frequency (transmit frequency). Fig. 8 shows the conversion factor as function of τ for L and X band and incidence angles of 30° and 60° . At X band, 60° , and a time lag of 5 ms, a velocity/phase factor of about $0.01 \text{ ms}^{-1}/\text{deg}$ is obtained, which results in phase ambiguities at velocity intervals of 3.6 m/s. At a time lag of 1 ms, a phase difference of 1° corresponds to a velocity interval of about 0.05 m/s, and ambiguities occur only every 18 m/s. In view of the fact that modern ATI systems can resolve phase differences of less than 1° [J. Moreira, personal communication] and that an accuracy of measured currents of 0.05 m/s should usually be sufficient, we conclude that the choice of the ATI time lag is not very critical as far as velocity resolution and ambiguity problems are concerned.

V. SUMMARY AND CONCLUSION

In this paper, we have presented an advanced composite surface scattering model which is capable of simulating Doppler spectra of microwave backscatter from the ocean surface. The model is based on the simple expressions of Bragg scattering theory and requires significantly less computation time than more fundamental models which are based explicitly on Maxwell's equations. We have shown that Doppler spectra obtained from the proposed model agree well with predictions of the well-established fundamental model described in [6]. We conclude from the good agreement that both models can be

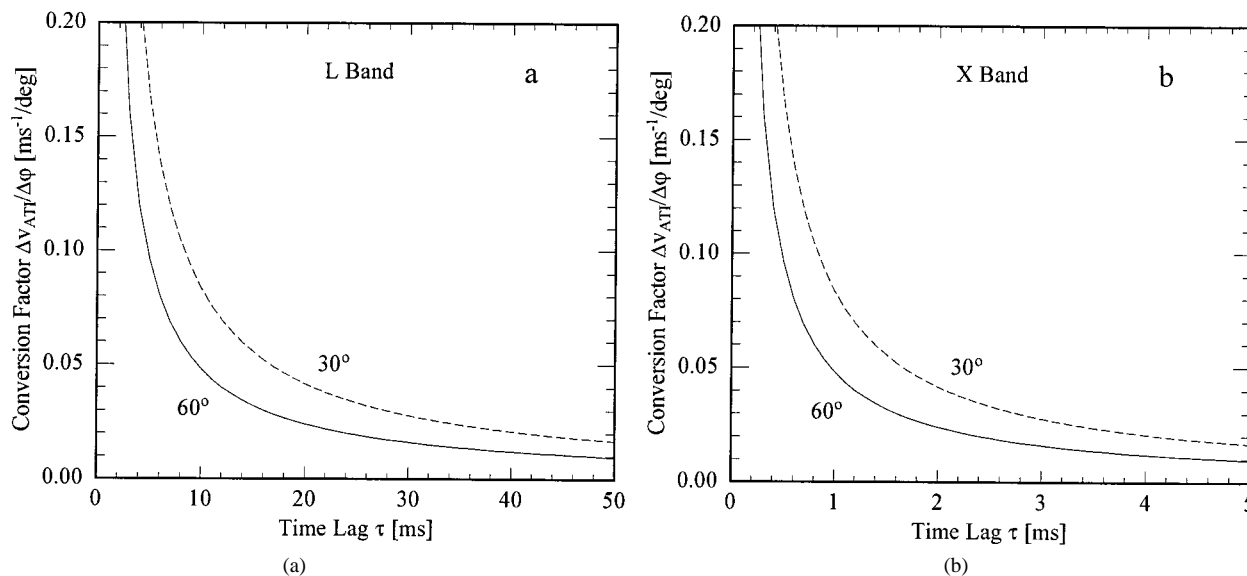


Fig. 8. ATI velocity/phase difference conversion factor as function of time lag τ and for incidence angles of 30° and 60°: (a) *L* band and (b) *X* band.

used equivalently for practical applications, where a reduction of computation times by more than an order of magnitude is a clear advantage of the proposed model.

Doppler models are required for the interpretation of along-track interferometric synthetic aperture radar (ATI) data which include information on surface currents. To investigate theoretical possibilities and limitations of current measurements by ATI and to determine favorable parameters of ATI systems, we have simulated Doppler and ATI velocity signatures for a variety of scenarios. It has been found that ATI-derived current fields can differ significantly from actual current fields if inadequate parameter values are chosen, which is in qualitative agreement with experimental results. According to our model results, the most important parameters which determine the linearity of the imaging mechanism are the incidence angle and the ratio between flight altitude and platform velocity.

For best linearity, a high incidence angle like 60° should be chosen, and the ratio between flight altitude and platform velocity should be as small as possible. Furthermore, high radar frequency bands like *X* band (10 GHz) appear to be better suited for current measurements, although this is not as obvious as the advantages of high incidence angles and small “ R/V ” ratios. The dependence of simulated ATI velocity signatures on the radar polarization is small, but VV polarization is favorable in view of larger radar backscattering cross sections of the ocean surface and thus more backscattered power and a better signal-to-noise ratio. High wind speeds result in better linearity between the shape of actual current variations and Doppler velocity variations, but low wind speeds correspond to longer decorrelation times of the backscattered field and thus less statistical fluctuations of measured phase differences. Ideal wind speeds for current measurements by ATI should be between about 5 and 10 m/s. The ATI time lag should be chosen such that it is significantly shorter than the decorrelation time of the field but that the accuracy of measured phase and velocity variations is sufficient. We have presented diagrams of model results and simple analytical calculations which show

the relationship between time lag, autocorrelation of the field, and velocity resolution.

If both ATI antennas are used for transmitting and receiving in a dual-baseline setup, one can choose the antenna separation such that the short baseline/time lag ensures accurate phase and velocity measurements and the long time lag is long enough to determine the decay of the autocorrelation of the field, so that decorrelation time images can be generated according to a method described in [22].

Finally, the wind direction at a test site should be known in order to correct ATI velocities for the mean contribution associated with the orbital motions of ocean waves and with the phase velocities of the two Bragg wave components. It is not difficult to estimate this correction, but if the wind direction is not well known, this may result in an offset of all measured current components by as much as 0.5 m/s at *X* band and an incidence angle of 60°, the proposed best parameters for current measurements. However, some basic information on the wind vector should usually be available, and in many cases it can even be derived from signatures of features like wind streaks, wind generated waves, or surface films in a radar image itself [24].

Despite our finding that large incidence angles and high radar frequencies should be better suited for current measurements, current fields have already been extracted successfully from ATI data at *L* band and incidence angles as small as 30°, as described in [4]. This is consistent with our theory; an absence of obvious nonlinearities in the case discussed in [4] can be attributed to the fact that the current gradients in the test area were relatively small and did not change very rapidly in space. In the vicinity of small current gradients, the surface wave spectrum experiences only a weak hydrodynamic modulation. The relevance of our recommendation of a high incidence angle and a high radar frequency increases with the strength of the current gradients to be imaged, with wind speed, and with the spatial resolution of the radar and the required accuracy.

If the right parameters are chosen, along-track SAR interferometry should be well suited for oceanic current measurements.

After two overflights in perpendicular directions and a calculation of corrections with a theoretical model like the one proposed in this work, it should be possible to determine current fields within an area of a few square kilometers with a resolution of current variations better than 0.1 m/s and with a spatial resolution of a few meters. In principle, this is a much more direct way of measuring currents and current gradients than approaches based on conventional radar imagery, which rely on an interpretation of image intensity variations. The general feasibility of the ATI technique has already been demonstrated. We are currently planning experiments with new ATI systems designed on the basis of our suggestions, and we are looking forward to a comparison of simulated X band ATI signatures and actual experimental data in a follow-on publication.

REFERENCES

- [1] R. M. Goldstein and H. A. Zebker, "Interferometric radar measurement of ocean surface currents," *Nature*, vol. 328, pp. 707–709, 1987.
- [2] J. W. Wright, "A new model for sea clutter," *IEEE Trans. Antennas Propagat.*, vol. AP-16, pp. 217–223, 1968.
- [3] G. R. Valenzuela, "Theories for the interaction of electromagnetic and ocean waves—A review," *Bound. Layer Meteorol.*, vol. 13, pp. 61–85, 1978.
- [4] H. C. Graber, D. R. Thompson, and R. E. Carande, "Ocean surface features and currents measured with synthetic aperture radar interferometry and HF radar," *J. Geophys. Res.*, vol. 101, pp. 25 813–25 832, 1996.
- [5] D. R. Thompson and J. R. Jensen, "Synthetic aperture radar interferometry applied to ship-generated waves in the 1989 Loch Linnhe experiment," *J. Geophys. Res.*, vol. 98, pp. 10 259–10 269, 1993.
- [6] D. R. Thompson, "Calculation of microwave Doppler spectra from the ocean surface with a time-dependent composite model," in *Radar Scattering from Modulated Wind Waves*, G. J. Komen and W.A. Oost, Eds., Dordrecht, The Netherlands: Kluwer, 1989, pp. 27–40.
- [7] D. R. Lyzenga and J. R. Bennett, "Full-spectrum modeling of synthetic aperture radar internal wave signatures," *J. Geophys. Res.*, vol. 93, pp. 12 345–12 354, 1988.
- [8] R. Romeiser, W. Alpers, and V. Wismann, "An improved composite surface model for the radar backscattering cross section of the ocean surface—Part I: Theory of the model and optimization/validation by scatterometer data," *J. Geophys. Res.*, vol. 102, pp. 25 237–25 250, 1997.
- [9] W. J. Plant and W.C. Keller, "Evidence of Bragg scattering in microwave Doppler spectra of sea return," *J. Geophys. Res.*, vol. 95, pp. 16 299–16 310, 1990.
- [10] F. Feindt, J. Schröter, and W. Alpers, "Measurement of the ocean wave-radar modulation transfer function at 35 GHz from a sea-based platform in the North Sea," *J. Geophys. Res.*, vol. 91, pp. 9701–9708, 1986.
- [11] R. Romeiser and W. Alpers, "An improved composite surface model for the radar backscattering cross section of the ocean surface—Part II: Model response to surface roughness variations and the radar imaging of underwater bottom topography," *J. Geophys. Res.*, vol. 102, pp. 25 251–25 267, 1997.
- [12] R. Romeiser, A. Schmidt, and W. Alpers, "A three-scale composite surface model for the ocean wave-radar modulation transfer function," *J. Geophys. Res.*, vol. 99, pp. 9785–9801, 1994.
- [13] W. R. Alpers, D. B. Ross, and C.L. Rufenach, "On the detectability of ocean surface waves by real and synthetic aperture radar," *J. Geophys. Res.*, vol. 86, pp. 6481–6498, 1981.
- [14] W. Alpers and K. Hasselmann, "The two-frequency microwave technique for measuring ocean wave spectra from an airplane or satellite," *Bound. Layer Meteorol.*, vol. 13, pp. 215–230, 1978.
- [15] T. R. Larson, L. I. Moskowitz, and J. W. Wright, "A note on SAR imagery of the ocean," *IEEE Trans. Antennas Propagat.*, vol. AP-24, pp. 393–394, 1976.
- [16] W. R. Alpers and C. L. Rufenach, "The effect of orbital motions on synthetic aperture radar imagery of ocean waves," *IEEE Trans. Antennas Propagat.*, vol. AP-27, pp. 685–690, 1979.
- [17] K. Hasselmann, R. K. Raney, W. J. Plant, W. Alpers, R. A. Shuchman, D. R. Lyzenga, C. L. Rufenach, and M. J. Tucker, "Theory of synthetic aperture radar ocean imaging: A MARSEN view," *J. Geophys. Res.*, vol. 90, pp. 4659–4686, 1985.
- [18] R. O. Harger, "The side-looking radar image of time-variant scenes," *Radio Sci.*, vol. 15, pp. 749–756, 1980.
- [19] W. J. Plant and W. C. Keller, "The two-scale radar wave probe and SAR imagery of the ocean," *J. Geophys. Res.*, vol. 88, pp. 9776–9784, 1983.
- [20] D. R. Thompson, B. L. Gotwols, and W. C. Keller, "A comparison of K_u band Doppler measurements at 20° incidence with predictions from a time-dependent scattering model," *J. Geophys. Res.*, vol. 96, pp. 4947–4955, 1991.
- [21] A. W. Bjerkaas and F. W. Riedel, "Proposed model for the elevation spectrum of a wind-roughened sea surface," *Appl. Phys. Lab.*, p. 32, 1979.
- [22] R. E. Carande, "Dual baseline and frequency along-track interferometry," in *Dig. Int. Geoscience and Remote Sensing Symp. (IGARSS '92)*, 1992, pp. 1585–1588.
- [23] W. J. Plant, E. A. Terray, R. A. Pettit Jr., and W. C. Keller, "The dependence of microwave backscatter from the sea on illuminated area: Correlation times and lengths," *J. Geophys. Res.*, vol. 99, pp. 9705–9723, 1994.
- [24] P. D. Mourad, "Viewing a cold-air outbreak using satellite-based synthetic aperture radar and advanced very high resolution radiometer imagery," *J. Geophys. Res.*, vol. 101, pp. 16 391–16 400, 1996.



Roland Romeiser was born in Bremen, Germany, in 1966. He received the Diplom degree in physics from the University of Bremen in 1990 and the Dr.rer.nat. degree from the Institute of Oceanography, the University of Hamburg, Germany, in 1993.

He has wide experience in the remote sensing of ocean currents, waves, and winds by various microwave sensors. He has been involved in a number of international remote sensing projects and experiments. His current research focuses on the theoretical modeling of radar signatures of spatially varying ocean surface current and wind fields. From August 1998 through July 1999, he spent a year with Dr. D. R. Thompson at Applied Physics Laboratory, Johns Hopkins University, Laurel, MD, as a Feodor Lynen Fellow of the Alexander von Humboldt Gesellschaft. The final version of this paper was written within the framework of this exchange.



Donald R. Thompson received the B.S. degree in physics from Case Western Reserve University, Cleveland, OH, in 1964, and the Ph.D. degree in theoretical physics from the University of Minnesota, Minneapolis, in 1968.

He spent two years studying problems in stellar nucleosynthesis at the California Institute of Technology, Pasadena, before returning to the University of Minnesota in 1970. From 1976 to 1978, he was an Alexander von Humboldt Fellow in the Institute of Theoretical Physics at the University of Tübingen, Germany. In 1980, he joined Applied Physics Laboratory, Johns Hopkins University, Laurel, MD, where his research has been concerned with the physics of ocean surface waves and electromagnetic scattering from the ocean surface.